

# 3D Printing of Interdigitated Dielectric Elastomer Actuators

Alex Chortos, Ehsan Hajiesmaili, Javier Morales, David R. Clarke,\* and Jennifer A. Lewis\*

Dielectric elastomer actuators (DEAs) are soft electromechanical devices that exhibit large energy densities and fast actuation rates. They are typically produced by planar methods and, thus, expand in-plane when actuated. Here, reported is a method for fabricating 3D interdigitated DEAs that exhibit in-plane contractile actuation modes. First, a conductive elastomer ink is created with the desired rheology needed for printing high-fidelity, interdigitated electrodes. Upon curing, the electrodes are then encapsulated in a self-healing dielectric matrix composed of a plasticized, chemically crosslinked polyurethane acrylate. 3D DEA devices are fabricated with tunable mechanical properties that exhibit breakdown fields of  $25 \text{ V } \mu\text{m}^{-1}$  and actuation strains of up to 9%. As exemplars, printed are prestrain-free rotational actuators and multi-voxel DEAs with orthogonal actuation directions in large-area, out-of-plane motifs.

## 1. Introduction

Soft actuators exhibit actuation modes that mimic the capabilities and efficiencies of biological systems.<sup>[1]</sup> These active devices rely on phase change materials,<sup>[2,3]</sup> fluidic actuation,<sup>[4]</sup> or electrostatic attraction to achieve the desired motion of interest. Dielectric elastomer actuators (DEAs) utilize electrostatic forces that are generated by applying a voltage across an insulating elastomer sandwiched between two electrodes to drive their actuation. The force induced by attraction of opposite charges reduces the elastomer thickness in the direction of the electric field and leads to a concomitant expansion in orthogonal directions.<sup>[5,6]</sup> Since this external field can be applied and removed quickly, DEAs exhibit fast actuation rates and high efficiency<sup>[3,7]</sup> making them attractive for use in soft robotics,<sup>[8–13]</sup> tunable optical lenses,<sup>[14]</sup> and haptic interfaces.<sup>[15–17]</sup>

Most DEAs are fabricated by planar methods, such as spin coating<sup>[8,15,18]</sup> and sequential mechanical assembly,<sup>[19–22]</sup> and therefore expand in-plane when actuated (Figure 1a). With further processing, these planar structures can be transformed into bending actuators,<sup>[9]</sup> rolled actuators,<sup>[15]</sup> or prestrained systems using rigid frames.<sup>[10,11,23–25]</sup> For many applications of interest, contractile actuation is advantageous.<sup>[26–30]</sup> Yet prestrained DEAs provide contractile strains in only a small proportion of the total device area.<sup>[23,31,32]</sup> Moreover, these devices often exhibit impaired

cycling and breakdown behavior<sup>[33–35]</sup> and the presence of a rigid frame limits the geometries that can be achieved.<sup>[24,36]</sup> Recent attention has been directed toward developing approaches that enable contractile displacements in prestrain-free DEAs, including manual and automated stacking of individual planar layers<sup>[37]</sup> or sequential deposition of active materials via inkjet printing<sup>[38]</sup> and spray coating.<sup>[39]</sup> The fabrication of contractile actuators with vertically oriented electrodes offers a more promising approach (Figure 1b). While arrays of vertical electrodes can be patterned lithographically, new masks must be generated for each device design.<sup>[40–42]</sup> By contrast, 3D printing enables the rapid design and fabrication of soft materials in nearly arbitrary geometries.<sup>[43–47]</sup> For example, direct ink writing (DIW), an extrusion-based 3D printing method, has been used to pattern soft functional materials, including sensors,<sup>[48]</sup> stretchable electronics,<sup>[49]</sup> liquid crystalline elastomers,<sup>[50]</sup> and soft robots.<sup>[51,52]</sup> While this method has recently been used to print DEAs, they do not exhibit an in-plane contractile response.<sup>[52–54]</sup>

Here, we create 3D DEAs composed of interdigitated vertical electrodes that are printed, cured, and encapsulated in an insulating dielectric matrix (Figure 1c). These prestrain-free contractile DEAs can be produced in nearly arbitrary geometries. During their actuation, the stress generated is given by  $\sigma = \epsilon_0 \epsilon_r (E)^2$ , where  $\epsilon_0$  is the vacuum permittivity,  $\epsilon_r$  is the dielectric constant, and  $E$  is the electric field. For small strains, the actuation strain ( $s_z$ ) is  $s_z = \sigma / E_Y = \epsilon_0 \epsilon_r (E)^2 / E_Y$ , where  $E_Y$  is the Young's modulus. Their actuation performance is therefore maximized by increasing the breakdown field and dielectric constant, while simultaneously reducing the elastic modulus of the matrix. Since variations in the dielectric thickness can cause localization of the electric field that results in premature breakdown,<sup>[39]</sup> we optimized the DEA device performance by developing a conductive electrode ink with tailored rheological and printing behavior and a plasticized dielectric matrix that exhibits electrical self-healing.

## 2. Results and Discussion

### 2.1. Electrode Ink Design

We synthesized a versatile elastomer for use as the continuous phase in our conductive electrode ink via a step growth polymerization of ethylene glycol-based di-ene and dithiol small molecules (Figure 2a). Using this highly selective thiol-ene chemistry,<sup>[55]</sup> we prepared poly(ethylene glycol ethylene sulfide)

Dr. A. Chortos, E. Hajiesmaili, J. Morales, Prof. D. R. Clarke, Prof. J. A. Lewis  
John A. Paulson School of Engineering and Applied Sciences  
Harvard University  
29 Oxford Street, Cambridge, MA 02138, USA  
E-mail: clarke@seas.harvard.edu; jalewis@seas.harvard.edu

 The ORCID identification number(s) for the author(s) of this article can be found under <https://doi.org/10.1002/adfm.201907375>.

DOI: 10.1002/adfm.201907375

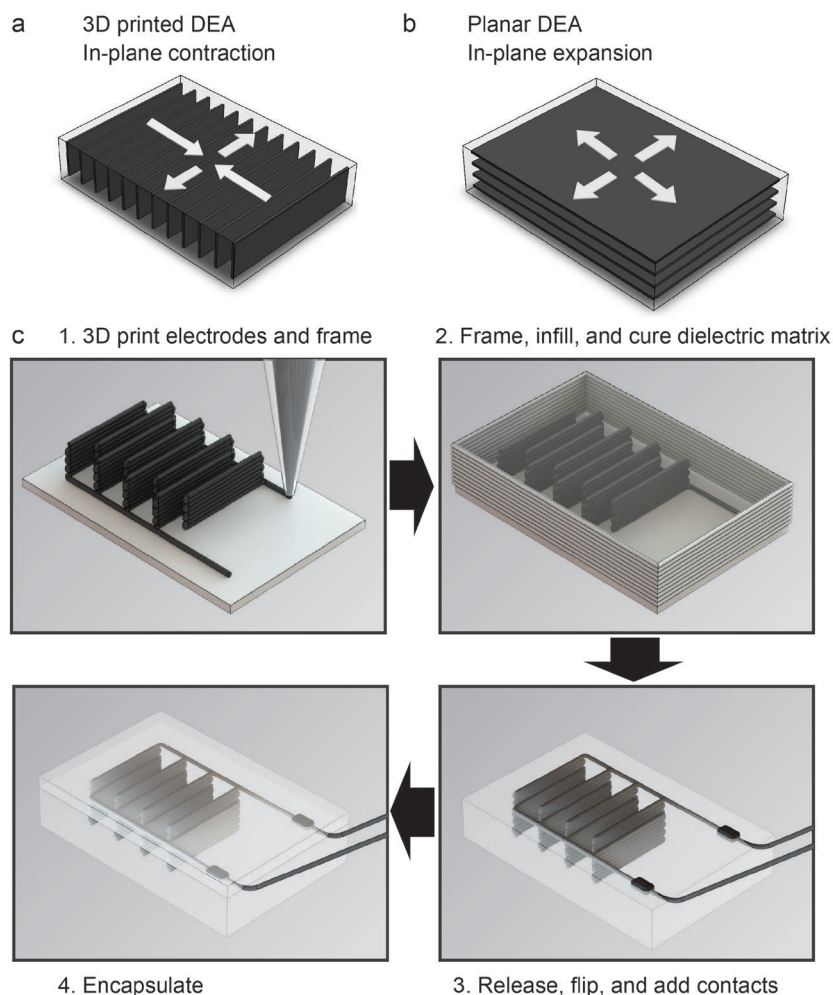


**Figure 1.** Schematic illustration of printed DEA devices with a) vertical and b) horizontal electrodes that give rise to in-plane contraction and expansion, respectively. c) Schematic illustration of the fabrication process for printing DEAs with high aspect ratio, interdigitated electrodes followed by dielectric matrix infilling.

(PEG-PES) oligomers terminated with vinyl ether groups. We refer to each oligomer produced using the ideal molecular weight based on initial stoichiometry. Using this nomenclature, PEG-PES<sub>1.7</sub> is an oligomer with an ideal number average molecular weight ( $M_n$ ) of 1.7 kDa (Table S1, Supporting Information). Similar to other thiol-ene compositions, the conversion of vinyl groups is greater than 95%, as measured by Fourier-transform infrared spectroscopy (Figure S1, Supporting Information).<sup>[56,57]</sup>

Next, we produced chemically crosslinked elastomers by mixing the PEG-PES oligomers with dithiol chain extenders and trithiol crosslinkers. This strategy of simultaneous chain extension and crosslinking<sup>[58]</sup> of low-molecular weight oligomers decouples their rheological and printing behavior in the uncured state from the final cured properties. The uncured viscosity is determined by the molecular weight of the oligomers ( $M_n$ ), while the cured elastic modulus is determined by the molecular weight between crosslinks ( $M_c$ ) (Figure 2a) according to the equation for entropic elasticity ( $E_Y = 3RT/M_c$ ).<sup>[59]</sup> Using PEG-PES oligomers with the same  $M_n$ , the  $M_c$  of the cured elastomer can be tuned by varying the ratio of difunctional

chain extenders to trifunctional crosslinkers, allowing the cured mechanical properties to be independently controlled from its uncured viscosity. For PEG-PES<sub>1.7</sub> oligomers,  $E_Y$  of the cured elastomer can be varied from  $\approx 0.5$  MPa for a dithiol:trithiol molar ratio of 12.67 to  $\approx 2.5$  MPa for an elastomer with trithiol crosslinkers (Figure 2b). While pure PEG crystallizes at room temperature,<sup>[60,61]</sup> the presence of the sulfur atoms along the PEG-PES oligomer backbone prevents crystallization, resulting in a low glass transition temperature ( $T_g$ ) of  $\approx -67$  °C (Figure S2, Supporting Information). Notably, unlike many elastomers created from low-viscosity precursors,<sup>[58,62,63]</sup> our PEG-PES elastomers exhibit excellent ultimate tensile properties, with ultimate tensile strength higher than 15 MPa for some compositions upon curing. They also exhibit large elongation at break (Figure S3a, Supporting Information), low plastic deformation, and minimal hysteresis (Figure S3b, Supporting Information). However, one drawback of using oligomers with low  $M_n$  is their low gel fraction at very low crosslinker concentrations (Figure S4, Supporting Information).

Printing vertical electrodes in high aspect ratio layouts requires a conductive ink with both shear thinning behavior and a high storage modulus ( $G'$ ) and low loss tangent.<sup>[64,65]</sup> Although a wide range of conductive inks has been reported previously,<sup>[49,66–74]</sup> carbon-filled inks are attractive for DEA fabrication due to their low density and cost, good stability, and ability to self-clear.<sup>[73,74]</sup> Hence, we incorporated carbon black particles into a PEG-PES oligomer solution (dithiol:trithiol molar ratio of 0.67),

which serve as both a conductive filler phase and a rheological modifier. From oscillatory shear measurements, we find that a 18 wt% carbon black loading yields sufficient values of  $G' \approx 65$  kPa and  $\tan \delta \approx 0.1$  (Figure S5, Table S2, Supporting Information) to enable filamentary printing. We find that increasing the  $M_n$  of the PEG-PES oligomer in these electrode inks (18 wt% carbon black) reduces their plateau  $G'$  and  $G''$  values, yet leads to a concomitant rise in these values once the shear yield stress is exceeded (Figure 2c).<sup>[75]</sup> Inks based on PEG-PES<sub>1.7</sub> oligomers lead to the most uniform printed electrodes, with minimal width variation at the ends of the printed electrodes (Figure 2d). After printing, the vertically oriented electrodes are thermally cured at 100 °C for several minutes (Figure S6, Supporting Information) resulting in an  $E_Y$  of 0.49 MPa (Figure 2d) and good cycling stability with minimal plastic deformation (Figure 2e and Figure S7, Supporting Information). An electrical conductivity of  $6.5 \text{ S m}^{-1}$  is measured for these printed and cured electrodes, which is sufficient for the capacitance to remain independent of frequency up to  $\approx 1000$  Hz (Figure S8, Supporting Information) with a low-field RC time constant of  $1.3 \times 10^{-3}$  s.

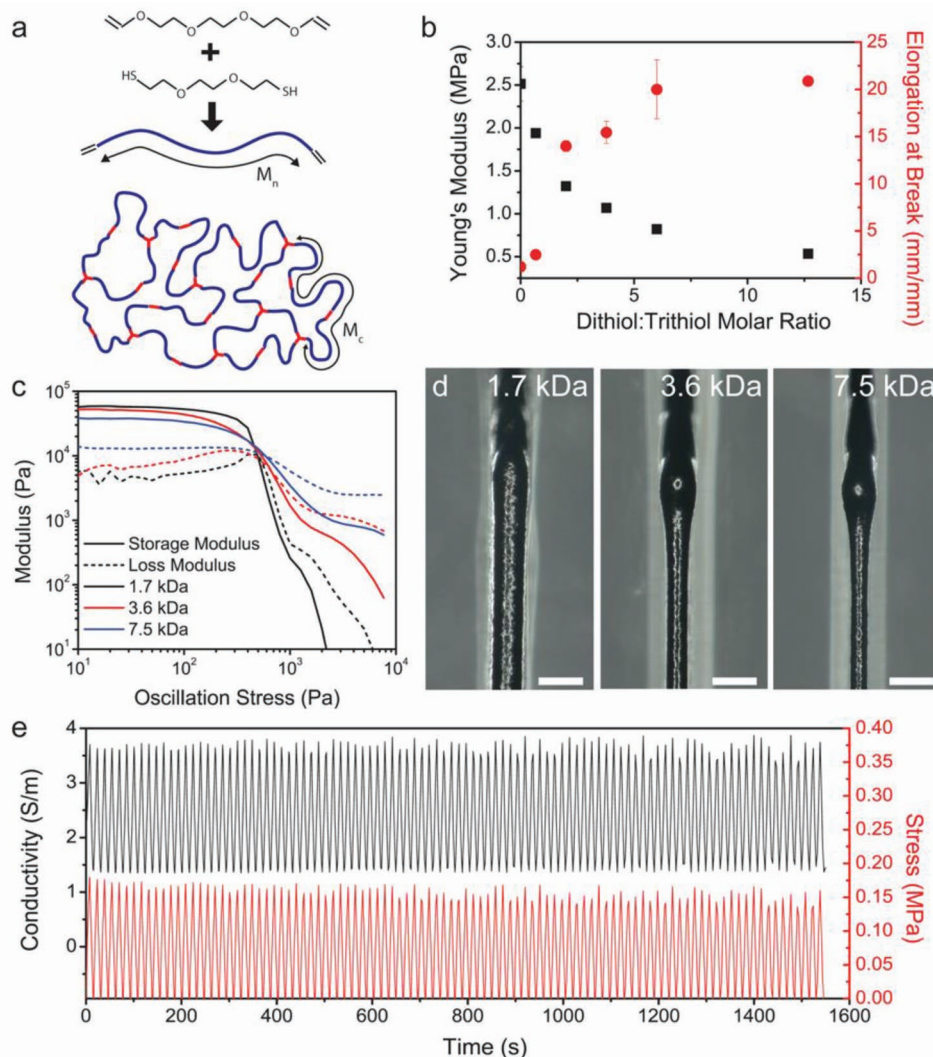


**Figure 2.** a) Synthesis of poly(ethylene glycol)-poly(ethylene sulfide) (PEG-PES) elastomers via chain extension and crosslinking. b) Young's modulus ( $E_Y$ ) and elongation at break for pure PEG-PES elastomers (without carbon black) with different chain extender-to-crosslinker ratios. c) Storage ( $G'$ ) and loss ( $G''$ ) moduli as a function of shear stress of electrode inks composed of PEG-PES thiol-ene elastomers with varying oligomer chain length filled with 18 wt% carbon black. d) Optical images of electrode traces printed through a 100  $\mu\text{m}$  nozzle that reveal the effect of PEG-PES oligomer molecular weight on the electrode width and bead formation. Scale bars are 200  $\mu\text{m}$ . e) Electrical conductivity of printed and cured electrodes during cyclic testing from 0% to 25% strain.

## 2.2. Dielectric Matrix Design

We encapsulated the printed electrodes within a self-healing dielectric matrix composed of a commercially available polyurethane diacrylate (PUA) oligomer,<sup>[8,34]</sup> which contains a low-molecular weight bifunctional crosslinker butanediol diacrylate (BDDA) and a plasticizer, dioctyl phthalate (DOP; **Figure 3a**). DOP reduces the uncured viscosity of the dielectric matrix, which facilitates its infilling between the printed electrodes. This plasticizer also reduces the mechanical loss tangent ( $\tan \delta$ ) of the cured dielectric matrix (**Figure 3b** and **Figure S9**, Supporting Information). Notably, the  $\tan \delta$  affects both the efficiency of electromechanical energy conversion<sup>[16,76]</sup> as well as the frequency response of the actuators.<sup>[15]</sup> For polyurethane-based elastomers, the mechanical losses in the dielectric matrix are influenced by hydrogen bonds between chains, which

dissipate energy by breaking and reforming during mechanical cycling. Plasticizers can disrupt these bonds thereby increasing chain mobility<sup>[77,78]</sup> and reducing mechanical losses. Notably, plasticized dielectric matrices exhibit improved stress relaxation (**Figure S10**, Supporting Information).

As the plasticizer:polymer ratio increases from 0 to 1.2, the dielectric constant of these matrices at 20 Hz increases from 5.31 to 6.01 (**Figure S11**, Supporting Information). DOP is known to have a relatively low conductivity compared to other plasticizers,<sup>[79]</sup> which results in dielectric matrices with low-frequency conductivity values that vary from  $1.6 \times 10^{10}$  to  $4.0 \times 10^{10}$   $\text{S m}^{-1}$  for 0:1 (pure polymer) to 1.2:1 plasticizer:polymer weight ratios (**Figure S11**, Supporting Information). Yet this plasticizer does not affect the crosslinking efficiency, as measured by the gel fraction (**Figure S12**, Supporting Information).

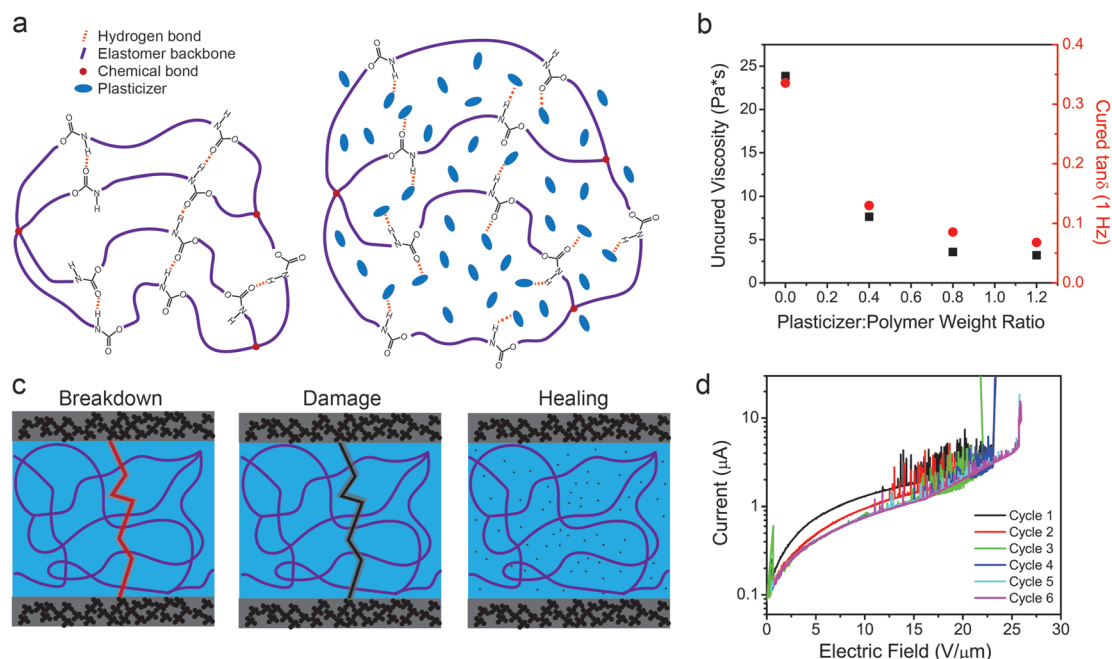


**Figure 3.** a) Low-shear viscosity (measured at  $1 \text{ s}^{-1}$ ) of uncured plasticized matrix plotted alongside the  $\tan \delta$  of the cured plasticized matrix with varying plasticizer-to-polymer ratios. b) Conceptual schematic showing the proposed mechanism for how the plasticizer improves the  $\tan \delta$  and stress relaxation by reducing the entanglements between chains. c) Schematic of the self-healing process for dielectrics composed of polymer and plasticizer. d) Several cycles to breakdown of a 3D DEA device, which is inflated with a dielectric matrix composed of 1.2:1 plasticizer:polymer ratio and 0.12:1 crosslinker-to-polymer ratio. A linear ramp rate of  $100 \text{ V s}^{-1}$  ( $0.26 \text{ V } \mu\text{m}^{-1} \text{ s}^{-1}$ ) is used ( $0.01 \text{ Hz}$  stimulation) to reduce the contribution of displacement currents to the measured current.

Beyond serving as a plasticizer, DOP acts as a mobile liquid that can heal the dielectric matrix after electrical breakdown. After a breakdown event occurs, DOP can diffuse from the surrounding region, allowing the device to return to a functional state (Figure 3c).<sup>[13,80]</sup> Figure 3d shows multiple actuation cycles until breakdown. The number of current spikes decreases with increasing cycles, suggesting that the electrodes exhibit self-clearing behavior that might arise from thermal decomposition of carbon black particles in regions with high leakage current.<sup>[73,81]</sup> The use of fault-tolerant actuator materials is particularly important in printed devices, since the DIW electrodes exhibit nonplanar sidewalls due to stacking of printed filamentary features (Figure S13, Supporting Information).

### 2.3. Printing and Performance of 3D DEA Devices

We printed 3D DEAs composed of interdigitated vertical electrodes via DIW and measured their in-plane contraction optically (Figure 4a). The ideal dielectric matrix should exhibit a large breakdown field with a small elastic modulus, since the maximum actuation strain ( $s_z$ ) during actuation is given by  $s_z = \epsilon_0 \epsilon_r (E_{EB})^2 / E_Y$ , where  $E_{EB}$  is the breakdown field of the dielectric matrix. However, the breakdown field typically exhibits a positive correlation with the elastic modulus.<sup>[82]</sup> To investigate this tradeoff between  $E_Y$  and  $E_{EB}$ , we varied the crosslinker (BDDA) concentration to tune the Young's modulus (Figure S14, Supporting Information). Printed DEAs with a dielectric matrix composed of 1.2:1 weight ratio of plasticizer:polymer and varying amounts of BDDA exhibit a

maximum actuation strain at a ratio of crosslinker:polymer of 0.04 (Figure 4b and Figure S15, Supporting Information). Their breakdown fields of  $20$  to  $28 \text{ V } \mu\text{m}^{-1}$  are comparable to those reported for DEAs using dielectric gels with similar Young's moduli and chemical composition.<sup>[83]</sup>

For devices with finite electrode stiffness, the actuation strain is limited by the stiffening effect of the electrodes.<sup>[22]</sup> To account for this effect, we used a simple analytical model to calculate the strain in the  $z$ -direction ( $s_z$ ) based on an effective modulus in the  $y$ - $z$  plane derived from the elastic modulus of the electrodes ( $E_{Y, \text{electrodes}}$ ), the fraction of electrodes in the device ( $\phi_{\text{electrodes}}$ ), the elastic modulus of the dielectric ( $E_{Y, \text{dielectric}}$ ), and the fraction of the dielectric ( $\phi_{\text{dielectric}}$ ) as given by

$$s_z = \frac{\epsilon_0 \epsilon_r \left(\frac{V}{d}\right)^2}{\phi_{\text{electrodes}} E_{Y, \text{electrodes}} + \phi_{\text{dielectric}} E_{Y, \text{dielectric}}} \quad (1)$$

where  $V$  is the voltage and  $d$  is the thickness of the dielectric. In a typical device with a pitch of  $500 \mu\text{m}$  and an electrode width of  $100 \mu\text{m}$ ,  $\phi_{\text{electrodes}}$  is  $0.2$  and  $\phi_{\text{dielectric}}$  is  $0.8$ . This simple analytical model assumes no constraints arising from the passive part of the dielectric matrix. We compared the analytical model to a finite element model (FEM; Figure 4c and Figure S16, Supporting Information) to quantify the effect of the passive area of the matrix on the actuation response. Based on the difference between the FEM and analytical model in Figure 3c, the passive constraints reduce the actuation strain by  $\approx 40\%$ . In future work, we plan to minimize this constraint by increasing the active area of the printed DEA devices. The FEM model predicts slightly higher actuation strains than observed

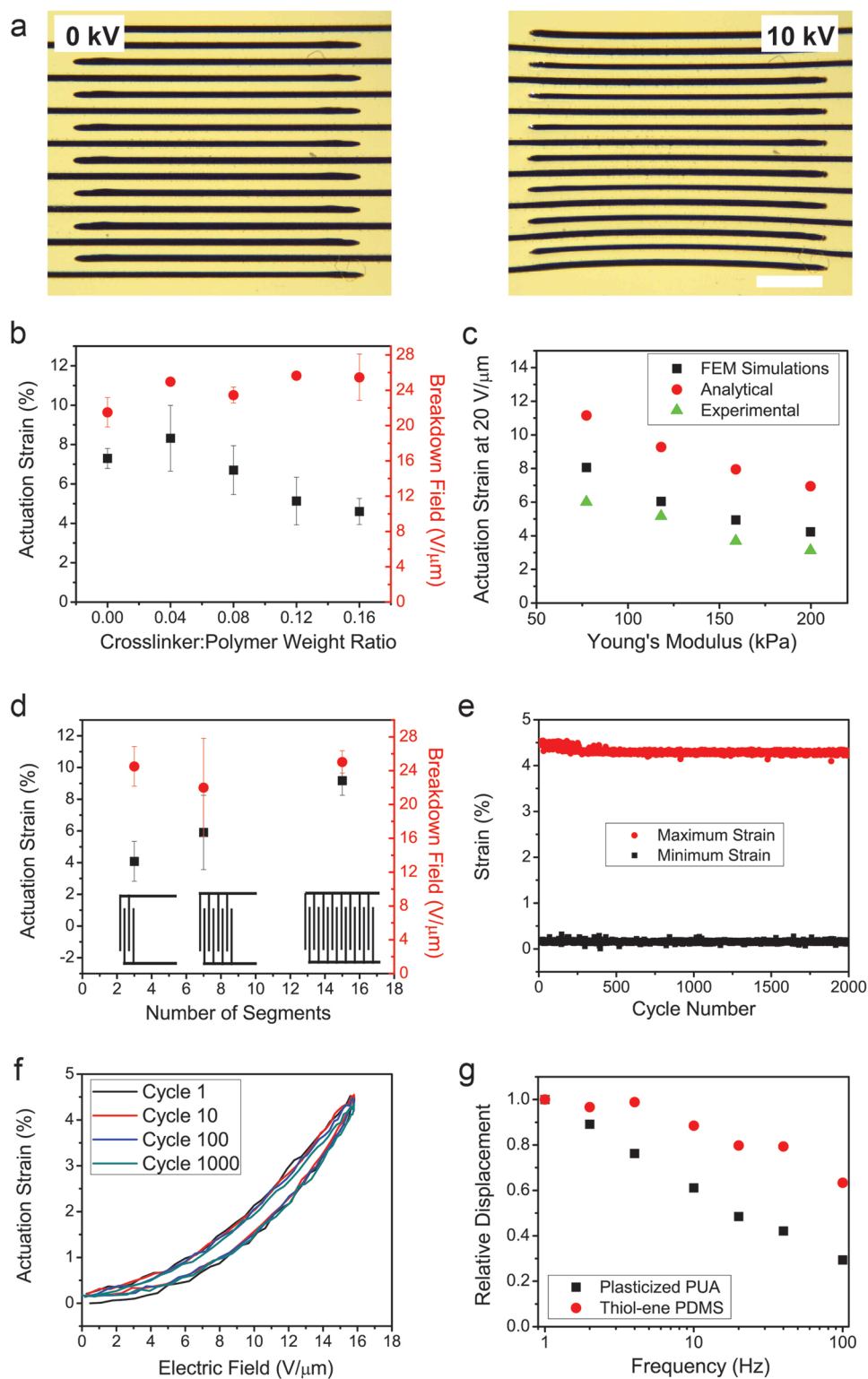


**Figure 4.** a) Representative images of a 3D DEA device during actuation showing an actuation strain of  $\approx 9\%$ . The white scale bar is 2 mm. (Note: The electrode height is  $800\ \mu\text{m}$  (10 layers), pitch is  $500\ \mu\text{m}$ , and overlap between interdigitated electrodes is  $8\ \text{mm}$ .) b) Actuation strain as a function of crosslinker-to-polymer ratio for dielectric matrices composed of 1.2:1 plasticizer-to-polymer ratio ( $n = 3$ ). c) Comparison of measured actuation strain to analytical calculations and FEM predictions. d) Actuation strain and breakdown field for 3D DEA devices with 3, 7, and 15 dielectric segments ( $n = 3$ ) for actuators with an electrode height of  $800\ \mu\text{m}$  (ten layers), pitch of  $500\ \mu\text{m}$ , and overlap between interdigitated electrodes of  $8\ \text{mm}$ . The samples were infiltrated with a dielectric matrix composed of 1.2:1 plasticizer:polymer ratio and 0.04:1 crosslinker:polymer ratio. e) Maximum and minimum actuation

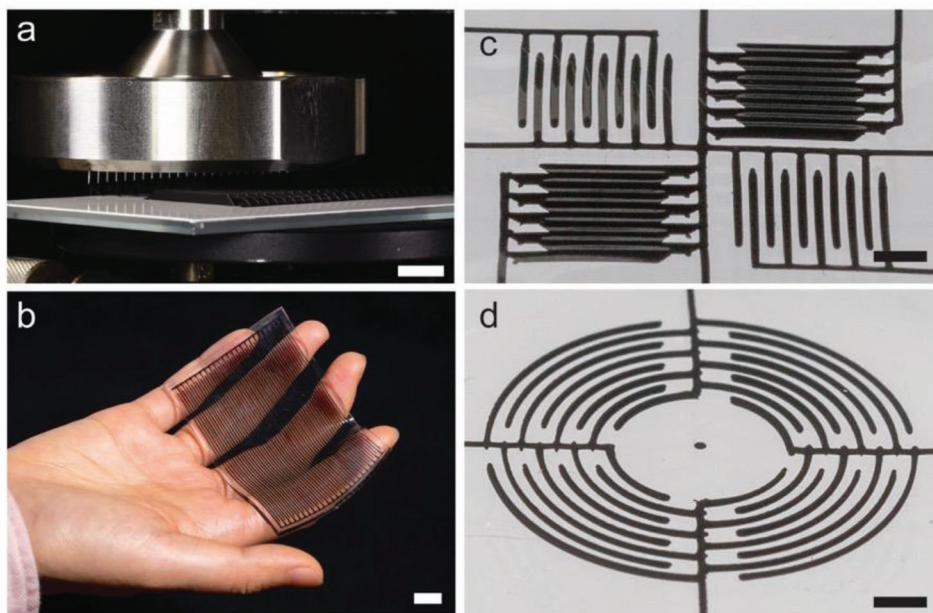


**Figure 5.** Optical images of a) a multinozzle printhead with 20 nozzles (200  $\mu\text{m}$  inner diameter) aligned in a 1D array with a center-to-center spacing between nozzles of 2 mm (scale bar = 10 mm). b) 3D DEA device composed of high-aspect ratio, interdigitated electrodes (1.5 mm in height) with a total active area of  $47 \times 75 \text{ mm}^2$  (scale bar = 10 mm). c) 3D DEA device composed of high-aspect ratio, interdigitated electrodes arranged in a quadrant architecture in which printed electrodes (0.48 mm in height) in the opposite diagonals are orthogonal to one another. Each quadrant occupies an area of  $5.0 \times 5.5 \text{ mm}^2$  and gives rise to an in-plane contraction in either the  $0^\circ$  or  $90^\circ$  direction (scale bar = 2 mm). d) 3D DEA device composed of high-aspect ratio, interdigitated electrodes (0.48 mm in height) arranged in an annular design in which each quadrant occupies a total active area of  $22 \text{ mm}^2$  and gives rise to rotational motion when the addressing electrodes are sequentially actuated (scale bar = 2 mm).

experimentally, because it uses idealized print geometries with an electrode width of  $100 \mu\text{m}$  (inner diameter of the nozzle) and a pitch of  $500 \mu\text{m}$ . In practice, the printed electrodes are roughly  $140 \mu\text{m}$  wide (Figure S13, Supporting Information), because the volumetric flow rate of ink exceeded that required to create features whose width corresponds to the nozzle size for the print speed used.

The print fidelity of the electrodes is particularly important when scaling to larger device sizes; print defects that result in locally thinner dielectric segments can reduce the breakdown field. In our 3D DEAs, as the number of dielectric segments increases from 3 to 7 to 15, the breakdown field remains  $\approx 25 \text{ V } \mu\text{m}^{-1}$ , while the actuation strain increases from 4.1% to 5.8% to 9.1%, respectively (Figure 4d). The increasing actuation strain is caused by the change in active area compared to passive constraints. Importantly, these devices exhibit consistent actuation over 2000 cycles (Figure 4e,f). Some drift during actuation cycling is common for DEAs with polar dielectrics<sup>[76,84]</sup> due to elastomer viscoelasticity or ion diffusion during large unipolar cycling of the applied voltage. We avoided this drift by using bipolar voltage waveforms.<sup>[13]</sup> Similar to other acrylate elastomers,<sup>[37]</sup> the strain amplitude of our acrylate-based actuators decreases with increasing frequency (Figure 4g). For comparison, we used polydimethylsiloxane (PDMS)

crosslinked using thiol-functionalized oligomers as a control matrix.<sup>[63]</sup> Those devices exhibited actuation strains of 9% and a breakdown field of  $\approx 26 \text{ V } \mu\text{m}^{-1}$  (Figure S17, Supporting Information) with a Young's modulus of 123 kPa. Those devices have improved frequency response (Figure 4g), albeit with a lower dielectric constant (and therefore lower actuation stress) and no self-healing behavior.

Using multinozzle DIW, we created 3D DEAs with large numbers of interpenetrating electrodes. Specifically, a commercial multinozzle printhead with 20 metal nozzles at a pitch of 2 mm is used (Figure 5a) to fabricate devices composed of 39 dielectric segments with a 1 mm pitch between electrodes (Figure 5b). Electrode arrays are printed to a height of 0.15 cm with an overlap of 7.5 cm between interdigitated electrodes to produce printed DEA devices with an active volume of  $0.15 \times 7.5 \times 3.9 \text{ cm}^3$ . These devices are printed within a few minutes at a print speed of  $2.5 \text{ mm s}^{-1}$ , which corresponds to an electrode fabrication rate approaching  $1 \text{ cm}^3 \text{ min}^{-1}$ . This additive fabrication method also enables one to pattern in-plane electric fields in different directions within a given device. For example, a 3D DEA with two sets of individually addressable orthogonal electrodes is fabricated that allows for in-plane contractile actuation (Figure 5c and Movies S3 and S4, Supporting Information). Similarly, we produced a rotational

strains for 2000 cycles of a 3D DEA device with an electrode height of  $800 \mu\text{m}$  (ten layers), pitch of  $500 \mu\text{m}$ , and overlap of 8 mm. The dielectric matrix is composed of 1.2:1 plasticizer:polymer ratio and 0.04:1 crosslinker:polymer ratio. f) Strain as a function of electric field for selected strain cycles during cycling. Cycling measurements were completed at 0.2 Hz. g) Actuation displacement as a function of frequency normalized to the displacement at 1 Hz. Actuation videos were collected at 2000 frames per second and videos were post-processed in Labview to extract the magnitude of deformation.

**Table 1.** Comparison of scalable fabrication methods for DEAs.

	Sequential spray-coating <sup>[44]</sup>	DIW bimorph <sup>[57]</sup>	HASEL <sup>[13,90]</sup>	Our work (PUA)	Our work (PDMS)
Dielectric thickness ( $\mu\text{m}$ )	80	500	1500	380	280
Dielectric constant	2.8	$\approx 3.5$	3.2	6.0	2.8
Operation voltage (kV)	4.5	5.5	26	10	7.5
Breakdown field ( $\text{V } \mu\text{m}^{-1}$ )	56	11	33	26	26
Actuation strain (%)	3.5	1.1 <sup>a)</sup>	10,79 <sup>b)</sup>	9	9
Actuation stress (kPa)	77	0.03	32	33	17
Energy density ( $\text{kJ m}^{-3}$ ) <sup>c)</sup>	1.4	0.091	94	7.15	1.14

<sup>a)</sup>Actuation strain is estimated from tip deflection and device dimensions<sup>[57]</sup>; <sup>b)</sup>10% strain is achieved using contractile actuation configuration,<sup>[90]</sup> while 79% strain is achieved in expansion configuration<sup>[13]</sup>; <sup>c)</sup>The energy density is calculated using the equation:  $U_e = \epsilon^2(V/d^4)/2E_{\text{dielectric}}$  for refs. [44,57] and our work, while it is estimated from the measured specific work for ref. [13].

actuator through sequential activation of four segments of interpenetrating electrodes printed in a cylindrically symmetric arrangement (Figure 5d and Movies S5 and S6, Supporting Information). Notably, previous DEA rotational actuators had to be fabricated using prestrained membranes,<sup>[85–87]</sup> due to limitations that arise from planar fabrication approaches. By using in-plane electric fields, we can generate contractile forces in free-standing elastomeric membranes that enable prestrain-free rotational actuators to be realized.

We compare the performance of our printed DEAs to those made by other fabrication methods, including spray-deposition,<sup>[39]</sup> multilayer DIW,<sup>[53]</sup> and hydraulically amplified (HASEL) actuators in Table 1.<sup>[13,88]</sup> Our devices exhibit comparable performance in terms of actuation strain and stress. However, compared to spray-deposition and multilayer filament printing, our method enables complex device layouts and multinozzle electrode printing. We note that further performance improvements may be possible by designing electrode inks that can be reliably printed through small nozzles ( $<10 \mu\text{m}$  in diameter) as well as improved dielectric materials.<sup>[89]</sup> Moreover, the use of embedded 3D printing<sup>[48]</sup> would allow patterning of DEAs with fully 3D electrodes in arbitrary geometries.

### 3. Conclusion

In summary, we have created 3D DEA devices via printing and matrix infilling that exhibit in-plane contractile actuation strains up to 9% with breakdown fields of  $\approx 25 \text{ V } \mu\text{m}^{-1}$ . Our additive fabrication method enables high-fidelity, interdigitated vertical electrodes to be patterned and seamlessly integrated with a self-healing dielectric matrix with tunable mechanical properties. To demonstrate the flexibility and scalability of this method, 3D DEAs were produced in the form of prestrain-free rotational actuators, multi-voxel DEAs with orthogonal actuation directions, and large-area, out-of-plane formats. These devices may find potential applications in soft robotics, somatosensory interfaces, and microfluidics.

### 4. Experimental Section

**Electrode Ink:** To produce an elastomeric matrix for the electrode inks, low molecular weight elastomeric oligomers were synthesized by combining tri(ethylene glycol) divinyl ether (PEG-dv, Aldrich) and

2,2'-(ethylenedioxy)diethanethiol (PEG-dt, Aldrich) at a total mass of 40 g in a 50 mL vial with 1 wt% of Irgacure 651 (I651) photoinitiator. The ratio of PEG-dv:PEG-dt was varied to control the molecular weight and viscosity of the resulting oligomeric species. The mass values of the three compositions and the molecular weight of their resulting oligomers are given in Table S1 in the Supporting Information. The solution was first stirred under nitrogen flow for 20 min to remove oxygen and dissolve the photoinitiator and then exposed to UV light for 15 min using an Omnicure S2000 UV source while stirring. The viscosity of the oligomers was characterized using a AR2000-EX rheometer with a 40 mm cone plate with a truncation angle of  $2^\circ$  and a gap of 56  $\mu\text{m}$ . A flow measurement was collected from 0.1 to  $10 \text{ s}^{-1}$  and showed Newtonian flow. The viscosity value was taken at  $1 \text{ s}^{-1}$ . IR absorbance measurements were collected using a Nicolet iS50 Spectrometer in an attenuated total reflection mode. A control calibration prepared using different concentrations of PEG-dv in  $200 \text{ g mol}^{-1}$  PEG showed a linear relationship between vinyl content and integrated vinyl peak intensities from 1560 to  $1670 \text{ cm}^{-1}$ . Gel permeation chromatography in tetrahydrofuran at  $25^\circ \text{C}$  and a flow rate of  $1.00 \text{ mL min}^{-1}$  was performed on a Waters Alliance HPLC 2695 with Agilent PLgel mini mixed-D columns. Samples were prepared at a concentration of  $2 \text{ mg mL}^{-1}$ . Refractive index (Wyatt Optilab rEX), photodiode array (Watter 2996 PDA), viscometer (Wyatt ViscoStar), and low-angle light scattering (Wyatt DAWN HELEOS II, 663.1 nm laser) detectors were used for determination of the  $dn/dc$ , polymer absolute molecular weight, and molecular weight distribution, respectively.

To create the electrode inks, carbon black particles (Ace Black 100 from Soltex) were added to the PEG-PES oligomer solution and mixed for 30 min in a Flacktec speedmixer. In a typical composition, 4 g of PEG-PES oligomeric species were combined with 0.88 g of carbon black to prepare electrode inks composed of 18 wt% carbon black. 1 wt% of 2,2'-azobisisobutyronitrile (AIBN), a thermal initiator, was then added to the ink using a stock solution composed of 20 wt% AIBN in chloroform. The ink was mixed for an additional 20 min in an uncapped state to facilitate chloroform evaporation. Finally, a 2,2'-(ethylenedioxy)diethanethiol (dithiol) chain extender and trimethylolpropane tris(3-mercaptopropionate) (trithiol, Aldrich) crosslinker were added to the ink, which was then mixed for an additional 5 min. For a typical ink composition, 4 g of PEG-PES-dv oligomer and 0.88 g of carbon black were combined with 0.21 g of dithiol and 0.30 g of trithiol. Electrode inks were loaded into 3 mL syringes (Nordson EFD) and centrifuged to remove any trapped air. Representative electrode traces were printed at a speed of  $3.0 \text{ mm s}^{-1}$  and pressure of 315 psi for the 1.7 kDa ink, at a speed of  $1.3 \text{ mm s}^{-1}$  and pressure of 500 psi for the 3.6 kDa ink, and a speed of  $0.4 \text{ mm s}^{-1}$  and pressure of 500 psi for the 7.5 kDa ink to evaluate their geometric and bead formation characteristics. Rheological measurements were performed using an AR-2000EX rheometer (TA Instruments) under ambient conditions equipped with a 40 mm stainless steel plate with a gap of 0.3 mm. After lowering the top plate, each sample was allowed to settle for 300s before the measurement.

Oscillatory measurements were carried out at a frequency of 1 Hz in the range of 1–10 000 Pa. To determine the glass transition temperature, differential scanning calorimetry (DSC) measurements were carried using a heat-cool-heat cycle between 0 and –90 °C, starting at the load temperature of 40 °C. Due to instrument limitations, cooling ramps were performed at 3 °C min<sup>-1</sup> and heating ramps at 10 °C min<sup>-1</sup>.

**Dielectric Matrix:** To produce the dielectric matrix, 5.45 g of polyurethane acrylate oligomer (CN9021, Sartomer) and 6.55 g of DOP plasticizer were combined in a 20 mL scintillation vial. BDDA was added to achieve the desired ratio of BDDA:polymer. For example, 0.22 g of BDDA was added to the mixture to achieve a crosslinker:polymer ratio of 0.04:1. Next, 1 wt% of 2,2-dimethoxy-1,2-diphenylethane-1-one (Irgacure 651, 1651) was added to the uncured matrix. Finally, the solution was mixed using a Flacktek speedmixer for 30 min to dissolve the initiator.

Comparison dielectrics composed of PDMS were prepared by combining 10 g of Sylgard 184 base with 2.5 g of a thiol-functionalized crosslinker ([5% (mercaptopropyl) methylsiloxane]-dimethylsiloxane copolymer from Gelest) and 0.1 g of 2-hydroxy-2-methylpropiophenone as a photoinitiator. The solution was mixed for 5 min in a Flacktek speedmixer.

Gel fraction measurements were performed by soaking a known weight of material in a 1:1 solvent mixture of acetone:dichloromethane for 72 h while replacing the solvent every 12 h. The gel fraction was defined as the mass of the remaining crosslinkable material (CN9021 and BDDA) divided by the initial mass of crosslinkable material.

**Mechanical Testing:** Representative samples of dielectric matrix material (3 mm thick) were prepared by casting CN9021:DOP:BDDA:1651 solution into a polyethylene dish. Under nitrogen, the samples were exposed to 395 nm light for 5 min to crosslink the elastomeric matrix. Circular samples (20 mm diameter) were produced using a mechanical punch. Dynamic mechanical analysis measurements were carried out using an AR-2000EX rheometer (TA Instruments) equipped with stainless steel parallel plates with 20 mm diameter. Samples were loaded to 2% compressive axial strain. Measurements were performed with a constant shear strain of 2%, while the frequency was increased from 0.1 to 100 Hz at a rate of 6 s per step.

To prepare samples of the PEG-PES elastomer for tensile testing, 12 g of PEG-PES oligomers were added to a 20 mL scintillation vial. 120 mg of 1651 was added to the mixture and mixed for 30 min to dissolve the initiator. Dithiol and trithiol were added in the desired ratio and mixed for 1 min. The mixture was poured into plastic petri dishes and degassed in vacuum ( $\approx$ 70 kPa) for 20 min to remove air bubbles. In nitrogen atmosphere, the samples were exposed to 395 nm light for 5 min to crosslink the films. The final films had thicknesses  $\approx$ 1 mm. Dog bone samples were cut using a laser cutter to have a neck length of 30 mm and a neck width of 5.0 mm. Tensile stress–strain curves were performed using an Instron 5566. Samples were measured with a crosshead speed of 1 mm s<sup>-1</sup> (0.04 mm mm s<sup>-1</sup>). The strain was defined as the length of the neck of the dog bone divided by the crosshead displacement, which might give rise to inaccurate strain values at large strains.

To prepare samples of the dielectric matrix for tensile testing, 12 g CN9021:DOP:BDDA:1651 mixtures were poured into plastic petri dishes and degassed in vacuum ( $\approx$ 70 kPa) for 20 min to remove air bubbles. In nitrogen atmosphere, the samples were exposed to 395 nm light for 5 min to crosslink the elastomer films. The final films had thicknesses  $\approx$ 1 mm. Dog bone samples were cut using a laser cutter to have a neck length of 30 mm and a neck width of 5.0 mm. Tensile stress–strain curves were performed using an Instron 5566. Samples were measured with a crosshead speed of 1 mm s<sup>-1</sup> (0.04 mm mm s<sup>-1</sup>). The strain was defined as the length of the neck of the dog bone divided by the crosshead displacement, which might give rise to inaccurate strain values at large strains. Measurements of stress relaxation and hysteresis were performed by first stretching to 0.5 mm mm<sup>-1</sup> strain at a rate of 5 mm s<sup>-1</sup> (0.2 mm mm s<sup>-1</sup>), holding the strain for 120 s, and releasing back to 0 strain at a rate of 1 mm s<sup>-1</sup>. The stress relaxation was quantified as the proportion of peak stress after 60 s of relaxation. The hysteresis was quantified as the full width of the difference in the strain at the half-maximum of the stress divided by the strain range.

**Device Fabrication:** Each DEA device was prepared by first spin coating a thin sacrificial layer of 5 wt% dextran in water onto a glass substrate followed by drying at 60 °C for 2 h. Next, the electrode ink was printed using an Aerotech 3D printer through a commercial 100  $\mu$ m nozzle from Nordson EFD onto the coated substrate at a printing speed of 2.5 mm s<sup>-1</sup>. The ink was printed in the form of high aspect-ratio, interdigitated electrodes. Next, a stiff PDMS ink (Momentive LSR 2080) was printed using the Aerotech printer through a 400  $\mu$ m nozzle around each of the electrode architectures to form a frame to contain the liquid dielectric. The printed electrodes and frame were cured for 1 h at 110 °C on a vacuum hotplate ( $-$ 70 kPa). Finally, the dielectric resin was cast within the frame, degassed for 20 min, and cured under nitrogen using 395 nm light for 5 min. The resulting DEA devices were soaked in deionized water for 20 min to dissolve the dextran layer and release them from the substrate.

Representative interdigitated DEA devices were fabricated with an electrode height of 800  $\mu$ m (ten layers), a pitch of 500  $\mu$ m, and an overlap of 8 mm between interdigitated electrodes. For rotational actuators and voxelated actuators, the electrode height was 480  $\mu$ m (six layers) and pitch was 500  $\mu$ m. For actuators printed using a multinozzle array, the electrode height was 1500  $\mu$ m (ten layers) and pitch was 1000  $\mu$ m. Electrical contacts were made to each embedded electrode by affixing steel wires using a commercial silver epoxy (Chemtronics CW 2400). Finally, a 100  $\mu$ m layer of dielectric was spin-coated as an encapsulation layer and cured under nitrogen using 395 nm UV light for 5 min.

**Device Testing:** The actuation strains of 3D-printed DEA devices were measured optically using a Point Grey automation camera and images were analyzed in real-time using a Labview program. For quasi-static measurements (Figure 4b,d), the ramp rate was 100 V s<sup>-1</sup>. All error bars represented one standard deviation. Cycling measurements in Figure 4e,f were conducted at 0.2 Hz to enable real-time optical measurement of the strains. To measure the frequency response of the devices, optical measurements were collected with a Fastcam MINI from Photron. Video was collected with a frame rate of 2000 frames per second, and the videos were postprocessed in Labview to extract the displacement of the actuator in each frame.

**FEM Simulations:** FEM simulations were carried out using Abaqus with a user subroutine element that incorporated the coupling terms of the stiffness matrix and the residual term due to the Maxwell stress. Simulation of dielectric elastomers required a coupled electro-mechanical analysis, where the mechanical and electrical governing equations were the balance of momentum and Gauss's flux theorem. The balance of momentum was coupled to the electric fields through Maxwell stress and the Gauss's flux theorem was coupled to the mechanical deformation due to the change of geometry. In these simulations, a nearly incompressible neo-Hookean material model and linear polarization model were used as the mechanical and electrical constitutive equations, respectively.

## Supporting Information

Supporting Information is available from the Wiley Online Library or from the author.

## Acknowledgements

The authors gratefully acknowledge support from the National Science Foundation through the Harvard MRSEC (grant no. DMR-1420570). J.A.L. and A.C. also acknowledge support from the Vannevar Bush Faculty Fellowship Program sponsored by the Basic Research Office of the Assistant Secretary of Defense for Research and Engineering and funded by the Office of Naval Research Grant N00014-16-1-2823 as well as the generous donation from the GETTYLAB in support of their work. This work made use of the Shared Experimental Facilities supported in part by the MRSEC Program of the National Science Foundation under

award number DMR-1419807. Finally, the authors thank L. K. Sanders for assistance with scientific photography, M. Duduta and H. Zhao for useful discussions, and E. Davidson for DSC experiments.

## Conflict of Interest

J.A.L. is a co-founder of Voxel8, Inc., a multi-material 3D printing company.

## Keywords

3D printing, dielectric elastomers, soft actuators, stretchable conductors

Received: September 5, 2019

Published online:

- 
- [1] S. M. Mirvakili, I. W. Hunter, *Adv. Mater.* **2018**, *30*, 1704407.
- [2] D. L. Thomsen, P. Keller, J. Naciri, R. Pink, H. Jeon, D. Shenoy, B. R. Ratna, *Macromolecules* **2001**, *34*, 5868.
- [3] A. Miriyev, K. Stack, H. Lipson, *Nat. Commun.* **2017**, *8*, 596.
- [4] R. F. Shepherd, F. Ilievski, W. Choi, S. A. Morin, A. A. Stokes, A. D. Mazzeo, X. Chen, M. Wang, G. M. Whitesides, *Proc. Natl. Acad. Sci. U. S. A.* **2011**, *108*, 20400.
- [5] R. Pelrine, R. Kornbluh, Q. Pei, J. Joseph, *Science* **2000**, *287*, 836.
- [6] P. Brochu, Q. Pei, *Macromol. Rapid Commun.* **2010**, *31*, 10.
- [7] S. I. Rich, R. J. Wood, C. Majidi, *Nat. Electron.* **2018**, *1*, 102.
- [8] M. Duduta, R. J. Wood, D. R. Clarke, *Adv. Mater.* **2016**, *28*, 8058.
- [9] S. Shian, K. Bertoldi, D. R. Clarke, *Adv. Mater.* **2015**, *27*, 6814.
- [10] E.-F. M. Henke, S. Schlatter, I. A. Anderson, *Soft Rob.* **2017**, *4*, 353.
- [11] C. T. Nguyen, H. Phung, T. D. Nguyen, H. Jung, H. R. Choi, *Sens. Actuators, A* **2017**, *267*, 505.
- [12] G.-Y. Gu, J. Zhu, L.-M. Zhu, X. Zhu, *Bioinspiration Biomimetics* **2017**, *12*, 011003.
- [13] E. Acome, S. K. Mitchell, T. G. Morrissey, M. B. Emmett, C. Benjamin, M. King, M. Radakovitz, C. Keplinger, *Science* **2018**, *359*, 61.
- [14] A. She, S. Zhang, S. Shian, D. R. Clarke, F. Capasso, *Sci. Adv.* **2018**, *4*, eaap9957.
- [15] H. Zhao, A. M. Hussain, M. Duduta, D. M. Vogt, R. J. Wood, D. R. Clarke, *Adv. Funct. Mater.* **2018**, *28*, 1804328.
- [16] K. Jun, J. Kim, I.-K. Oh, *Small* **2018**, *14*, 1801603.
- [17] H. Phung, P. T. Hoang, C. T. Nguyen, T. D. Nguyen, H. Jung, U. Kim, H. R. Choi, presented at *2017 IEEE/RSJ Int. Conf. Intelligent Robots and Systems (IROS)*, Vancouver, Canada, September **2017**.
- [18] P. Lotz, M. Matysek, H. F. Schlaak, *IEEE/ASME Trans. Mechatronics* **2011**, *16*, 58.
- [19] S. Rosset, O. A. Araromi, S. Schlatter, H. R. Shea, *J. Visualized Exp.* **2016**, *108*, 53423.
- [20] G. Kovacs, L. Düring, S. Michel, G. Terrasi, *Sens. Actuators, A* **2009**, *155*, 299.
- [21] D. McCoul, S. Rosset, N. Besse, H. R. Shea, *Smart Mater. Struct.* **2017**, *26*, 025015.
- [22] A. Poulin, S. Rosset, H. R. Shea, *Appl. Phys. Lett.* **2015**, *107*, 244104.
- [23] S. Rosset, O. A. Araromi, H. R. Shea, *Extreme Mech. Lett.* **2015**, *3*, 72.
- [24] J. Rossiter, P. Walters, B. Stoimenov, *Proc. SPIE* **2009**, *7287*, 72870H.
- [25] S. Hau, G. Rizzello, S. Seelecke, *Extreme Mech. Lett.* **2018**, *23*, 24.
- [26] M. Giousouf, G. Kovacs, *Smart Mater. Struct.* **2013**, *22*, 104010.
- [27] M. Imboden, E. de Coulon, A. Poulin, C. Dellenbach, S. Rosset, H. Shea, S. Rohr, *Nat. Commun.* **2019**, *10*, 834.
- [28] S. Rosset, A. Poulin, A. Zollinger, M. Smith, H. Shea, *Proc. SPIE* **2017**, *10163*, 101630P.
- [29] C. T. Nguyen, H. Phung, T. D. Nguyen, C. Lee, U. Kim, D. Lee, H. Moon, J. Koo, H. R. Choi, *Smart Mater. Struct.* **2014**, *23*, 065005.
- [30] H. S. Jung, K. H. Cho, J. H. Park, S. Y. Yang, Y. Kim, K. Kim, C. T. Nguyen, H. Phung, P. T. Hoang, H. Moon, J. C. Koo, H. R. Choi, *Smart Mater. Struct.* **2018**, *27*, 075011.
- [31] A. Poulin, M. Imboden, F. Sorba, S. Grazioli, C. Martin-Olmos, S. Rosset, H. Shea, *Sci. Rep.* **2018**, *8*, 9895.
- [32] B. M. O'Brien, E. P. Calius, T. Inamura, S. Q. Xie, I. A. Anderson, *Appl. Phys. A* **2010**, *100*, 385.
- [33] Y. Zhang, C. Ellingford, R. Zhang, J. Roscow, M. Hopkins, P. Keogh, T. McNally, C. Bowen, C. Wan, *Adv. Funct. Mater.* **2019**, *29*, 1808431.
- [34] X. Niu, H. Stoyanov, W. Hu, R. Leo, P. Brochu, Q. Pei, *J. Polym. Sci., Part B: Polym. Phys.* **2013**, *51*, 197.
- [35] A. Iannarelli, M. G. Niasar, *Proc. SPIE* **2017**, *10163*, 1016326.
- [36] J. Zhang, J. Sheng, C. T. O'Neill, C. J. Walsh, R. J. Wood, J. Ryu, J. P. Desai, M. C. Yip, *IEEE Trans. Rob.* **2019**, *35*, 761.
- [37] M. Duduta, E. Hajiesmaili, H. Zhao, R. J. Wood, D. R. Clarke, *Proc. Natl. Acad. Sci. USA* **2019**, *116*, 2476.
- [38] J. Maas, D. Tepel, T. Hoffstadt, *Meccanica* **2015**, *50*, 2839.
- [39] O. Araromi, A. Conn, C. Ling, J. Rossiter, R. Vaidyanathan, S. Burgess, *Sens. Actuators, A* **2011**, *167*, 459.
- [40] G. K. Lau, J. F. L. Goosen, F. V. Keulen, P. J. French, P. M. Sarro, *J. Micromech. Microeng.* **2006**, *16*, S35.
- [41] A. P. Gerratt, B. Balakrishnan, I. Penskiy, S. Bergbreiter, *Smart Mater. Struct.* **2014**, *23*, 055004.
- [42] M. Corbaci, W. Walter, K. Lamkin-Kennard, *Actuators* **2018**, *7*, 73.
- [43] R. L. Truby, J. A. Lewis, *Nature* **2016**, *540*, 371.
- [44] D. M. Vogt, K. P. Becker, B. T. Phillips, M. A. Graule, R. D. Rotjan, T. M. Shank, E. E. Cordes, R. J. Wood, D. F. Gruber, *PLoS One* **2018**, *13*, e0200386.
- [45] M. Jäntschi, S. Wittmeier, K. Dalamagkidis, A. Panos, F. Volkart, A. Knoll, presented at *2013 13th IEEE-RAS Int. Conf. Humanoid Robots (Humanoids)*, Atlanta, GA, October **2013**.
- [46] C. Tawk, M. in het Panhuis, G. M. Spinks, G. Alici, *Soft Rob.* **2018**, *5*, 685.
- [47] Y. L. Kong, M. K. Gupta, B. N. Johnson, M. C. McAlpine, *Nano Today* **2016**, *11*, 330.
- [48] J. T. Muth, D. M. Vogt, R. L. Truby, Y. Mengüç, D. B. Kolesky, R. J. Wood, J. A. Lewis, *Adv. Mater.* **2014**, *26*, 6307.
- [49] A. D. Valentine, T. A. Busbee, J. W. Boley, J. R. Raney, A. Chortos, A. Kotikian, J. D. Berrigan, M. F. Durstock, J. A. Lewis, *Adv. Mater.* **2017**, *29*, 1703817.
- [50] A. Kotikian, R. L. Truby, J. W. Boley, T. J. White, J. A. Lewis, *Adv. Mater.* **2018**, *30*, 1706164.
- [51] A. Kotikian, C. McMahan, E. C. Davidson, J. M. Muhammad, R. D. Weeks, C. Daraio, J. A. Lewis, *Sci. Rob.* **2019**, *4*, eaax7044.
- [52] R. L. Truby, M. Wehner, A. K. Grosskopf, D. M. Vogt, S. G. M. Uzel, R. J. Wood, J. A. Lewis, *Adv. Mater.* **2018**, *30*, 1706383.
- [53] G. Haghighashtiani, E. Habtour, S.-H. Park, F. Gardea, M. C. McAlpine, *Extreme Mech. Lett.* **2018**, *21*, 1.
- [54] A. H. Zamanian, D. A. Porter, P. Krueger, E. Richer, presented at *ASME 2018 Dynamic Systems and Control Conf.*, Atlanta, GA, September–October **2018**.
- [55] C. E. Hoyle, C. N. Bowman, *Angew. Chem., Int. Ed.* **2010**, *49*, 1540.
- [56] N. B. Cramer, T. Davies, A. K. O'Brien, C. N. Bowman, *Macromolecules* **2003**, *36*, 4631.
- [57] N. B. Cramer, S. K. Reddy, A. K. O'Brien, C. N. Bowman, *Macromolecules* **2003**, *36*, 7964.
- [58] J. M. Sirrine, V. Meenakshisundaram, N. G. Moon, P. J. Scott, R. J. Mondschein, T. F. Weiseman, C. B. Williams, T. E. Long, *Polymer* **2018**, *152*, 25.
- [59] J. D. Davidson, N. C. Goulbourne, *J. Mech. Phys. Solids* **2013**, *61*, 1784.

- [60] C. Wang, L. Feng, H. Yang, G. Xin, W. Li, J. Zheng, W. Tian, X. Li, *Phys. Chem. Chem. Phys.* **2012**, *14*, 13233.
- [61] W. Wang, X. Yang, Y. Fang, J. Ding, *Appl. Energy* **2009**, *86*, 170.
- [62] P. Mazurek, S. Vudayagiri, A. L. Skov, *Chem. Soc. Rev.* **2019**, *48*, 1448.
- [63] T. Wallin, J. Pikul, S. Bodkhe, B. Peele, B. Mac Murray, D. Therriault, B. McEnerney, R. Dillon, E. Giannelis, R. Shepherd, *J. Mater. Chem. B* **2017**, *5*, 6249.
- [64] K. Sun, T.-S. Wei, B. Y. Ahn, J. Y. Seo, S. J. Dillon, J. A. Lewis, *Adv. Mater.* **2013**, *25*, 4539.
- [65] J. E. Smay, J. Cesarano, J. A. Lewis, *Langmuir* **2002**, *18*, 5429.
- [66] S.-Z. Guo, K. Qiu, F. Meng, S. H. Park, M. C. McAlpine, *Adv. Mater.* **2017**, *29*, 1701218.
- [67] U. Daalkhajav, O. D. Yirmibesoglu, S. Walker, Y. Mengüç, *Adv. Mater. Technol.* **2018**, *3*, 1700351.
- [68] J. F. Christ, N. Aliheidari, A. Ameli, P. Pötschke, *Mater. Des.* **2017**, *131*, 394.
- [69] S. J. Leigh, R. J. Bradley, C. P. Purcell, D. R. Billson, D. A. Hutchins, *PLoS One* **2012**, *7*, e49365.
- [70] K. Fu, Y. Wang, C. Yan, Y. Yao, Y. Chen, J. Dai, S. Lacey, Y. Wang, J. Wan, T. Li, *Adv. Mater.* **2016**, *28*, 2587.
- [71] V. G. Rocha, E. Garcia-Tunon, C. Botas, F. Markoulidis, E. Feilden, E. D'Elia, N. Ni, M. Shaffer, E. Saiz, *ACS Appl. Mater. Interfaces* **2017**, *9*, 37136.
- [72] J. Wang, Y. Liu, Z. Fan, W. Wang, B. Wang, Z. Guo, *Adv. Compos. Hybrid Mater.* **2019**, *2*, 1.
- [73] W. Yuan, L. B. Hu, Z. B. Yu, T. Lam, J. Biggs, S. M. Ha, D. J. Xi, B. Chen, M. K. Senesky, G. Grüner, Q. Pei, *Adv. Mater.* **2008**, *20*, 621.
- [74] S. Rosset, H. R. Shea, *Appl. Phys. A* **2013**, *110*, 281.
- [75] Q. Zhang, L. A. Archer, *Langmuir* **2002**, *18*, 10435.
- [76] S. Michel, X. Q. Zhang, M. Wissler, C. Löwe, G. Kovacs, *Polym. Int.* **2010**, *59*, 391.
- [77] N. Ning, S. Li, H. Sun, Y. Wang, S. Liu, Y. Yao, B. Yan, L. Zhang, M. Tian, *Compos. Sci. Technol.* **2017**, *142*, 311.
- [78] N. Ning, B. Yan, S. Liu, Y. Yao, L. Zhang, T. W. Chan, T. Nishi, M. Tian, *Smart Mater. Struct.* **2015**, *24*, 032002.
- [79] M. Ali, T. Hirai, *J. Mater. Sci.* **2012**, *47*, 3777.
- [80] S. Hunt, T. G. McKay, I. A. Anderson, *Appl. Phys. Lett.* **2014**, *104*, 113701.
- [81] G.-K. Lau, S.-L. Chua, L.-L. Shiao, A. W. Y. Tan, *Proc. SPIE* **2012**, *8340*, 834016.
- [82] L. Yu, A. L. Skov, *Macromol. Rapid Commun.* **2018**, *39*, 1800383.
- [83] P. H. Vargantwar, A. E. Özçam, T. K. Ghosh, R. J. Spontak, *Adv. Funct. Mater.* **2012**, *22*, 2100.
- [84] W. Hu, *Ph.D. Thesis*, University of California, Los Angeles **2015**.
- [85] I. A. Anderson, T. Hale, T. Gisby, T. Inamura, T. McKay, B. O'Brien, S. Walbran, E. P. Calius, *Appl. Phys. A* **2010**, *98*, 75.
- [86] R. Waché, D. N. McCarthy, S. Risse, G. Kofod, *IEEE/ASME Trans. Mechatronics* **2015**, *20*, 975.
- [87] B. M. O'Brien, T. G. McKay, T. A. Gisby, I. A. Anderson, *Appl. Phys. Lett.* **2012**, *100*, 074108.
- [88] N. Kellaris, V. G. Venkata, G. M. Smith, S. K. Mitchell, C. Keplinger, *Sci. Rob.* **2018**, *3*, eaar3276.
- [89] D. M. Opris, *Adv. Mater.* **2018**, *30*, 1703678.
- [90] D. Kong, R. Pfattner, A. Chortos, C. Lu, A. C. Hinckley, C. Wang, W. Y. Lee, J. W. Chung, Z. Bao, *Adv. Funct. Mater.* **2016**, *26*, 4680.